S1. Range-folded echoes filtering

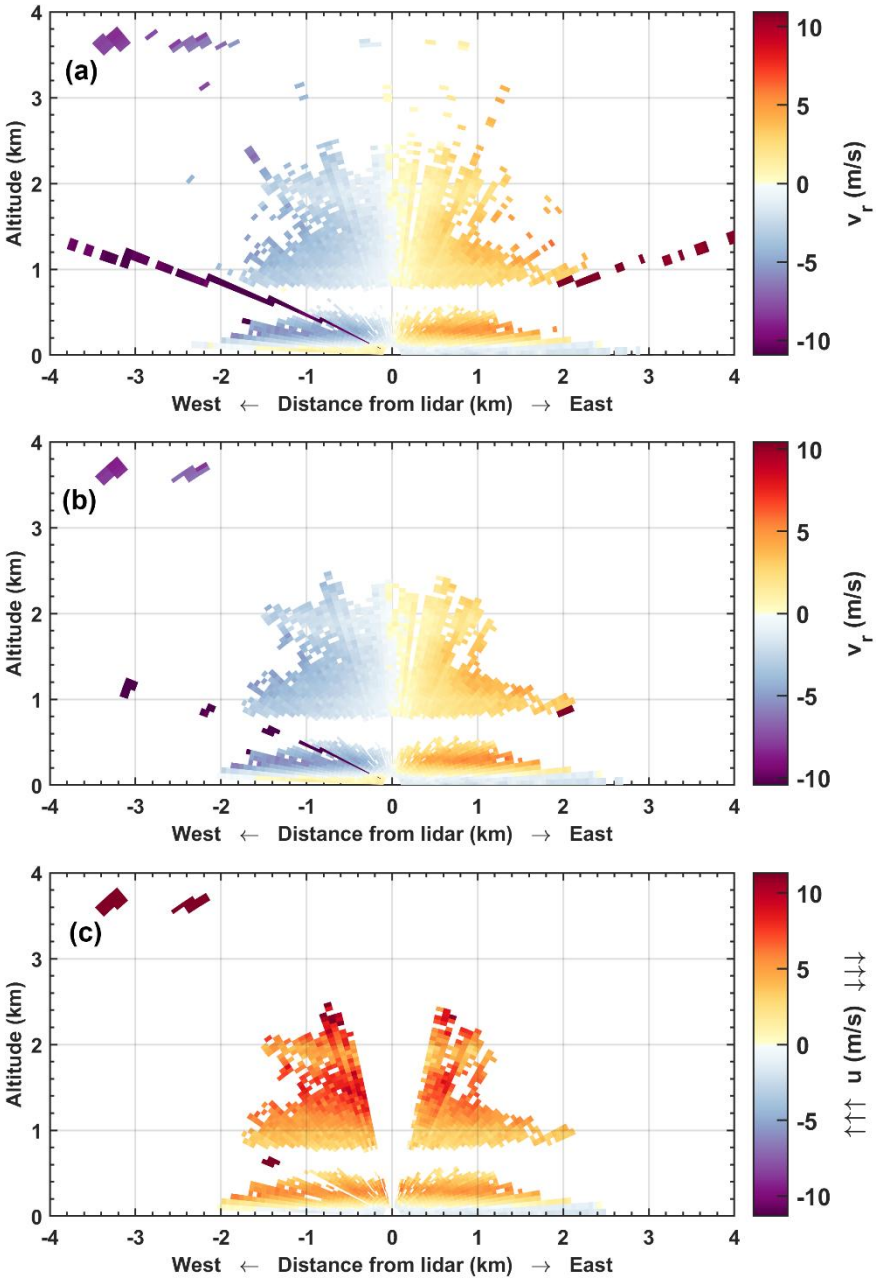

Figure S1. RHI scan recorded in Paris on October 31st around 00:28 UTC showing range-folded echoes from the cloud layer around 3.6 km altitude: (a) radial wind after quality filtering $\left(\mathrm{CNR} < -27\ dB;\ |v_r| > 30\ \mathrm{m \cdot s^{-1}};\ \sigma_{v_r} > 2.9\ \mathrm{m \cdot s^{-1}}\right)$, (b) radial wind after filtering isolated points, (c) zonal component of the wind after removing outliers in each horizontal layer. The few remaining spurious points will disappear when imposing a minimum number of points in each layer. The wind reconstruction result for this day is presented in Sec. S4.

S2. Wind reconstruction from non-perpendicular RHI scans

S2.1. Average wind

If α_1 and $\alpha_2$denote the azimuth of the two RHI scans of the pair, the angular opening between the scans will be $\beta = \alpha_2 - \alpha_1$ (assuming $\alpha_2 > \alpha_1$ yields $\beta > 0$). For each RHI scan, the horizontal wind is retrieved as described in Sec. 2.3.1, but it will be noted, in a more general way, v_1 and v_2 for the azimuths α_1 and α_2, respectively. The angles and the wind components are represented on Figure S2(a). The speeds v_1 and v_2 result from the projection of the zonal and meridional components u and v of the wind, following:

$$v_1 = u\,sin\,\alpha_1 + v\,cos\,\alpha_1 \quad \text{(S1.a)}$$

$$v_2 = u\,sin\,\alpha_2 + v\,cos\,\alpha_2 \quad \text{(S1.b)}$$

A linear combination of these equations, with some basic trigonometry, yields:

$$u = \frac{v_2 \cos\alpha_1 - v_1 \cos\alpha_2}{\sin\beta} \quad \text{(S2.a)}$$

$$v = \frac{v_1 \sin\alpha_2 - v_2 \sin\alpha_2}{\sin\beta} \quad \text{(S2.b)}$$

For a pair of perpendicular RHI ($\beta = 90°$) oriented in the cardinal directions ($\alpha_1 = 0°$ northward, and $\alpha_2 = 90°$ eastward), it is easy to verify that these formula simplify into $u = v_2$ and $v = v_1$, as can be deduced graphically from Figure S2(a).

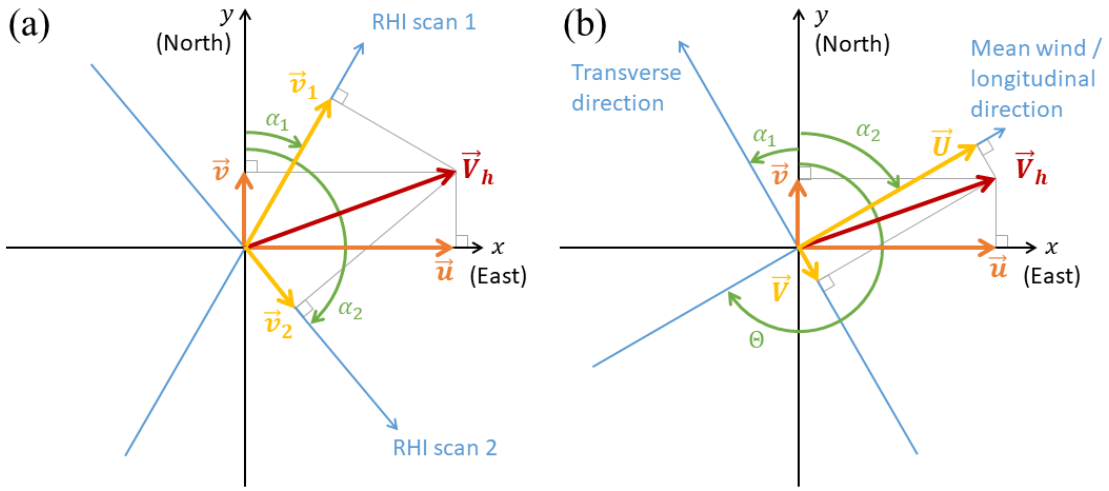

Figure S2. (a) Horizontal wind vector projection on non-perpendicular RHI scans. (b) Horizontal wind vector decomposition in the coordinate system aligned with the mean wind direction (here $\vec{V}_h$ is the instantaneous wind vector, that can deviate from the mean wind direction due to turbulence).

The speeds fields v_1 and v_2 from the two RHI scans are processed as described in Sec. 2.3.2 to derive layer-averages $\overline{v_1}$ and $\overline{v_2}$, then layer standard deviations σ_1 and σ_2. As averaging is a linear operation, the layer-averaged values $\bar{u}$ and $\bar{v}$ of the zonal and meridional components of the wind depend on $\overline{v_1}$ and $\overline{v_2}$ in the same way as in Eq. (S1.a). The horizontal wind speed V_h

and direction Θ can then be derived from $\bar{u}$ and $\bar{v}$ following the usual wind reconstruction equations (that are the same as for the DBS method):

$$V_h = \sqrt{\bar{u}^2 + \bar{v}^2} \quad \text{(S3.a)}$$

$$\Theta = 270° - \tan^{-1}\left(\frac{\bar{v}}{\bar{u}}\right) \quad \text{(S3.b)}$$

S2.2. Wind variances

For a function f of two partially correlated variables v_1 and v_2 affected by respective uncertainties σ_1 and σ_2 and with a covariance $\overline{v_1' v_2'}$, the error propagation formula predicts an uncertainty σ_f with:

$$\sigma_f^2 = \left(\frac{\partial f}{\partial v_1}\right)^2 \sigma_1^2 + \left(\frac{\partial f}{\partial v_2}\right)^2 \sigma_2^2 + 2\frac{\partial f}{\partial v_1} \cdot \frac{\partial f}{\partial v_2} \overline{v_1' v_2'} \quad \text{(S4)}$$

The zonal and meridional wind standard deviation σ_u and σ_v can thus be derived from Eq. (S2.a):

$$\sigma_u^2 = \frac{\sigma_1^2 \cos^2 \alpha_2 + \sigma_2^2 \cos^2 \alpha_1 - 2 \cos \alpha_1 \cos \alpha_2 \overline{v_1' v_2'}}{\sin^2 \beta} \quad \text{(S5.a)}$$

$$\sigma_v^2 = \frac{\sigma_1^2 \sin^2 \alpha_2 + \sigma_2^2 \sin^2 \alpha_1 - 2 \sin \alpha_1 \sin \alpha_2 \overline{v_1' v_2'}}{\sin^2 \beta} \quad \text{(S5.b)}$$

$\overline{v_1' v_2'}$ is the covariance between the wind components measured in the two RHI directions. This covariance cannot be determined using the cross-RHI method, so this term has to be neglected when rotating the variances. However, it was observed to be typically small compared to the others, based on ultrasonic anemometer observations (Bonin et al., 2017; Newman et al., 2016).

The computation of the wind variance in the wind-relative coordinate system correspond to a similar rotation problem (Figure S2.b): the second RHI scan would be oriented towards the mean wind (longitudinal direction), and the first RHI scan would be perpendicular to the mean wind (transverse direction). In this case, v_1 is the transverse wind component V and v_2 is the longitudinal wind component U, so that σ_1 is σ_V and σ_2 is σ_U. Besides, α_2 corresponds to the opposite of the mean wind direction, i.e. $\Theta - 180°$, while $\alpha_1 = \alpha_2 - 90°$ becomes $\Theta - 270°$ or $\Theta + 90°$. In that configuration, Eq. (S1.a) and (S1.a) become respectively:

$$U = -u \sin \Theta - v \cos \Theta \quad \text{(S6.a)}$$

$$V = u \cos \Theta - v \sin \Theta \quad \text{(S6.b)}$$

And then, the error propagation formula for partially correlated variables yields:

$$\sigma_U^2 = \overline{U'^2} = \overline{u'}^2 \sin^2 \Theta + \overline{v'}^2 \cos^2 \Theta + \overline{u'v'} \sin 2\Theta \quad \text{(S7.a)}$$

$$\sigma_V^2 = \overline{V'^2} = \overline{u'}^2 \cos^2 \Theta + \overline{v'}^2 \sin^2 \Theta - \overline{u'v'} \sin 2\Theta \quad \text{(S7.b)}$$

Again, the covariance term between the horizontal wind components will be neglected. The longitudinal wind standard deviation is of particular interest as it allows to compute the turbulent intensity, defined as $\mathrm{TI} = \sigma_U / \overline{U}$.

S3. Flow inclination retrieval

S3.1. Definition of the error function

At first, the error ε was defined as the average wind variance computed on all the layers with enough good-quality data points up to the top of the profile. One point to note, however, is that the exact number of good-quality data points in a given layer depends on the layers' inclination angle. In the bottom of the profile, where there are more than 150 points in each layer, the effect on the wind variance in the layer will be negligible. However, in the part of the profile where the number of points is just around the limit of 30, changing the layers' inclination angle will result in keeping or not a wind value in the layer. The normalization of the error by the number of layers with enough good-quality data points is therefore necessary to avoid jumps on the error curve as a function of the layers' tilt angle, that would create local minima in which the optimization algorithm could get trapped. Besides, the normalization also serves to obtain comparable error values at all time, no matter what the effective vertical range of the profile is.

Another point to consider is that the wind variance tends to be higher in the upper part of the profile, as the wind speed generally increases with altitude, so the upper layers have a higher weight in the error. As aid above, the wind variance in these layers is also the most sensitive to the layers' inclination angle, via the number of points included in the layer. It was therefore decided to compute the error only on a limited number of levels within the profile, in order to limit the noise on the error function. However, the performances of the horizontal TKE retrieval at altitudes that were not used for the optimization could be questioned, so different depth of the optimization layer were tested (Sec. 3.2.1). The error was defined using levels up to altitudes of 0.5 km, 1.0 km or 1.5 km, which corresponded respectively to 10, 20 or 30 layers in Paris, where the reconstructed profile had a vertical resolution of 50 m, and 20, 40 or 60 layers in Dunkerque, with a resolution of 25 m. Besides, the number of layers used to compute the error should not be too small, in order to get a smooth error function, so a minimum of 10 layers was used.

Figure S3 presents two examples RHI sweeps, with the two corresponding error curves as a function of the layers' tilt angle. These observations were recorded during a late summer sunny day in Paris, yielding a strong convective development of the PBL, with a nocturnal low-level jet on the two nights, and a constant north-easterly wind direction for the whole day. The time-altitude cross-section of the horizontal wind speed for this day can be found in Cheliotis et al. (2021). Figure S3(a) displays a RHI recorded in the nocturnal low-level jet, for which the error curve exhibits a marked minimum. Indeed, the strong wind shear around the layer causes a rapid increase of the wind variance when the binning layers do not follow the flow inclination. Conversely, Figure S3(b) correspond to a convective PBL case for which the error curve does not have a clear minimum. The curve amplitude is altogether smaller than for the LLJ case, and its marked fluctuations come from changes in the way that the binning layers intersect the convective structures.

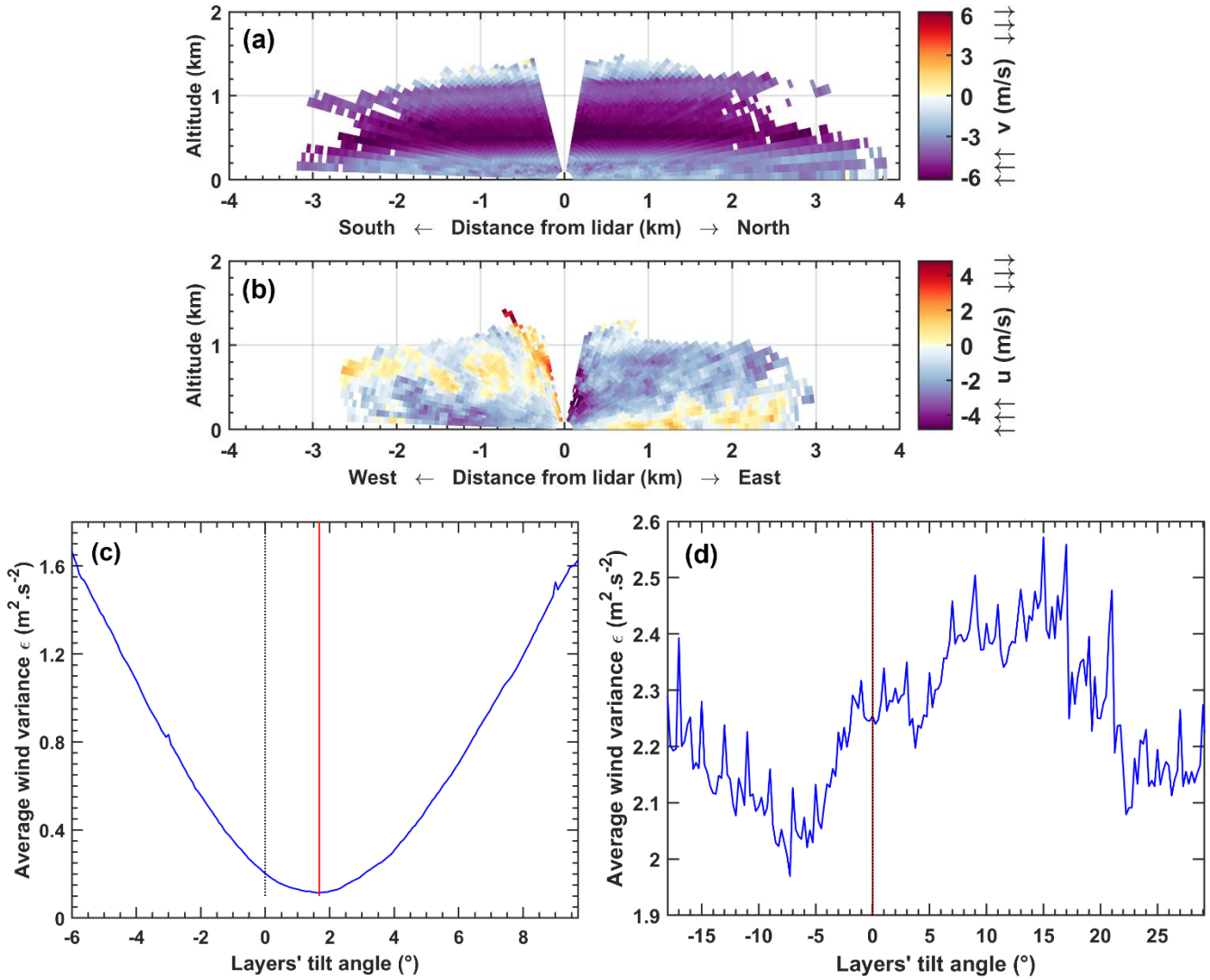

Figure S3. (a) Horizontal wind from the RHI scan recorded over Paris on September 9th 2014 around 01:58 UTC and (c) corresponding error curve as a function of the layers' inclination angle. (b) and (d) same for the RHI scan recorded over Paris on September 9th around 11:19 UTC. The black dotted and plain red vertical lines on panels (c) ad (d) respectively show the default/starting value and the optimized value of the layers' inclination.

S3.2. Parameterization of the optimization function `fminbnd`

The observation of the error curves obtained for RHI scans recorded in meteorological various situations showed that, in Paris, the inclination angle was typically comprised between −2° and +4°. The interval of inclination angles where to search for the minimum of the error function was therefore set to $[-6.00°; 9.70°]$, where the upper bound correspond to the absolute value of the lower bound, multiplied by the golden number. This takes advantage of the golden search algorithm principle (that cuts the search interval in two at each step, with the right side being wider than the left side by a ratio equal to the golden number)

in order to obtain an initial value of $\delta\varphi = 0°$ while keeping the asymmetry in the allowed values of $\delta\varphi$. Wider search intervals of $[-12.00°; 19.42°]$ and $[-18.00°; 29.12°]$ were also tested, to check if they allowed to retrieve the inclination in a larger number of cases without yielding to aberrant, too large values.

Prior to calling the optimization function, the error was computed for the edges of the search interval, and for the initial value of 0°. If the initial error value turned up to be larger than one of the edges error values, the optimization was not performed and the initial value of inclination was retained. When the optimization was performed, the tolerance parameter was set to 10^{-2}, which means convergence was reached when $\delta\varphi$ varied by less than 0.01° between two successive iterations. The number of iterations required was typically 13, which represents a significant, but tolerable increase of the computation time compared to a retrieval without layers' inclination (16 total calls to the error function for each RHI scan, instead of 1).

S3.3. Two-dimensional flow inclination

In this section, we suppose that the flow is composed of purely plane layers inclined in two dimensions from the horizontal. The line of steepest slope of the layers is oriented towards azimuth A (direction of the highest side) and the layers are inclined by an angle Φ (always positive). The unit vector $\vec{n}$ perpendicular to the flow layers is inclined by an angle Φ from the vertical (Figure S4.c), and oriented towards the azimuth A + 180° (Figure S4.a). Therefore, its coordinates in the zonal-meridional-vertical system, noted (x, y, z) on Figure S2, are $\vec{n} = (-\sin\Phi \sin A\,;\ -\sin\Phi \cos A\,;\ \cos\Phi)$.

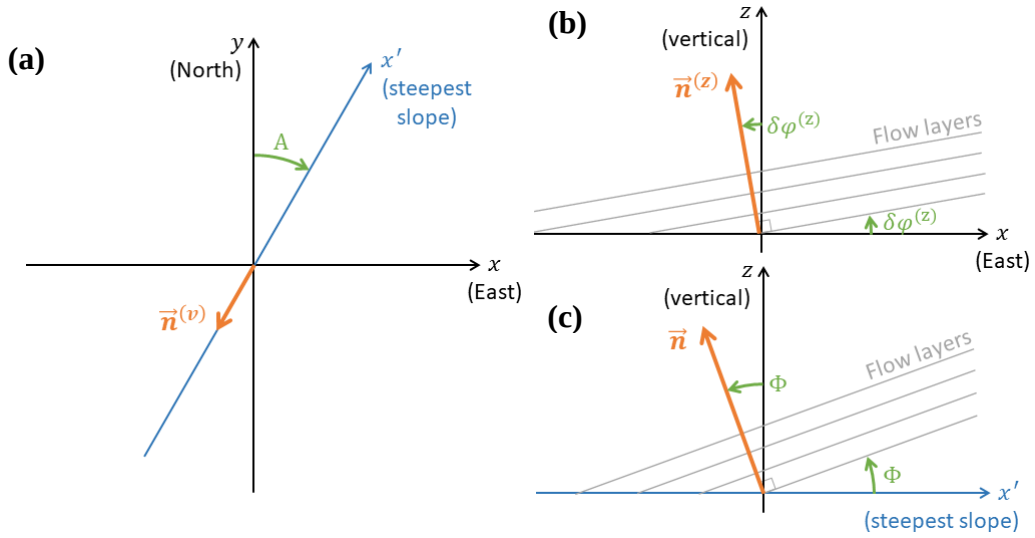

Figure S4. Projection of the unit vector $\vec{n}$ perpendicular to the flow layers (a) in the horizontal plane (projection $\vec{n}^{(v)}$), (b) in the vertical plan oriented in the zonal direction (projection $\vec{n}^{(z)}$) and (c) in the vertical plan oriented in the steepest slope direction.

The projection of this vector in a vertical plane oriented in the zonal direction is $\vec{n}^{(z)} = (-\sin\Phi \sin^2 A\,;\ 0;\ \cos\Phi)$ (Figure S4.b). This vector makes an angle $\delta\varphi^{(z)}$ with the vertical, which corresponds to the inclination of the averaging layers retrieved by the optimization procedure for the zonal RHI. Similarly, the projection of $\vec{n}$ in a vertical plane oriented in the meridional direction is $\vec{n}^{(m)} = (0;\ -\sin\Phi \cos^2 A\,;\ \cos\Phi)$, which corresponds to the inclination $\delta\varphi^{(m)}$ of the averaging layers retrieved

by the optimization procedure for the meridional RHI. Therefore, the tangent of the layers' inclination angles in each plane can be computed from the coordinates of $\vec{n}^{(z)}$ and $\vec{n}^{(m)}$:

$$\tan \delta\varphi^{(z)} = \frac{\sin \Phi \sin^2 \mathrm{A}}{\cos \Phi} = \tan \Phi \sin^2 \mathrm{A} \tag{C1a}$$

$$\tan \delta\varphi^{(m)} = \frac{\sin \Phi \cos^2 \mathrm{A}}{\cos \Phi} = \tan \Phi \cos^2 \mathrm{A} \tag{C1b}$$

For a line of steepest slope oriented from the North-East quadrant, i.e. $\mathrm{A} \in [0°; 90°]$, the two inclination angles $\delta\varphi^{(z)}$ and $\delta\varphi^{(m)}$ are positive, hence the withdrawal of the minus sign in the zonal or meridional coordinate when computing the tangent. The sum of these last two equations gives simply $\tan \Phi$, while the quotient gives the absolute value of $\tan \mathrm{A}$:

$$\tan \Phi = \tan \delta\varphi^{(z)} + \tan \delta\varphi^{(m)} \tag{C2a}$$

$$|\tan \mathrm{A}| = \sqrt{\frac{\tan \delta\varphi^{(z)}}{\tan \delta\varphi^{(m)}}} \tag{C2b}$$

As for the wind direction computation from $\bar{u}$ and $\bar{v}$ (S3), a two-argument tangent function is actually used, that will directly place A in the proper quadrant depending on the sign of its cosine and sine values (that have the same sign as $\delta\varphi^{(m)}$ and $\delta\varphi^{(z)}$, respectively).

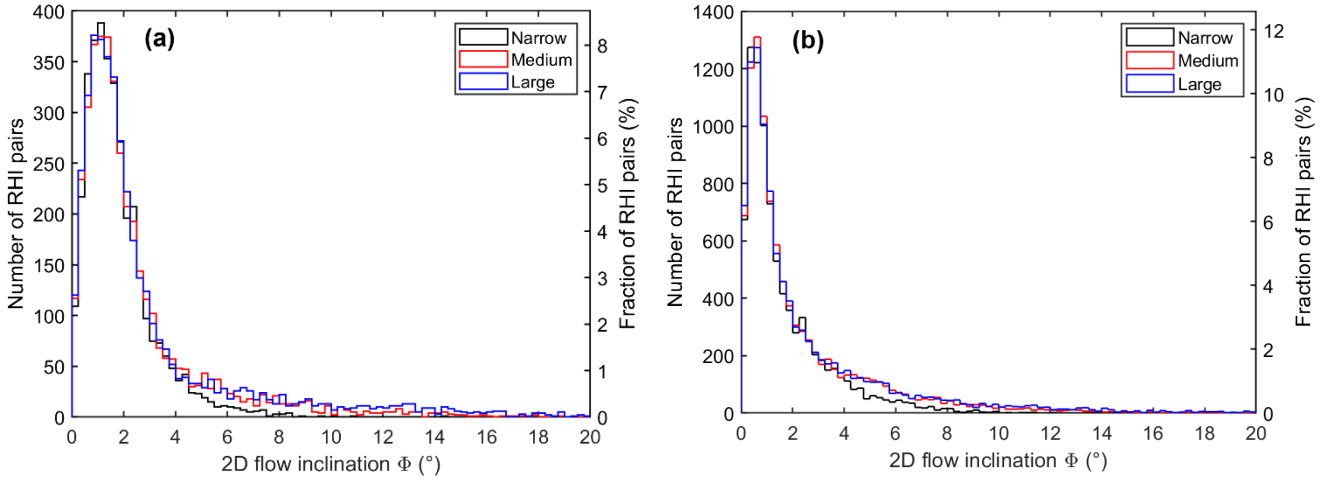

Figure S5. Distribution of the two-dimensional inclination angle Φ depending on the search interval for the sites of (a) Paris and (b) Dunkerque.

Figure S5 features the distribution of the two-dimensional inclination angle Φ on the two sites, while Figure S6 presents the rose of the two-dimensional inclination. In Paris, the flow was most frequently inclined towards the North-West or the North-East directions (Figure S6.a), while the most common wind directions were from the South-East to South-West, or from the North-East (Figure S6.b). In Dunkerque, the flow inclination was most frequently oriented towards the South-East, with secondary contributions towards the South-West and North-East (Figure S6.c), while the wind blew mostly from the South-West during the study period (Figure S6.d). As the coastline is oriented from the South-South-West to the North-East (with

the land at the southern side and very little orography), flow inclinations from the South-East direction follow the global inclination of the terrain.

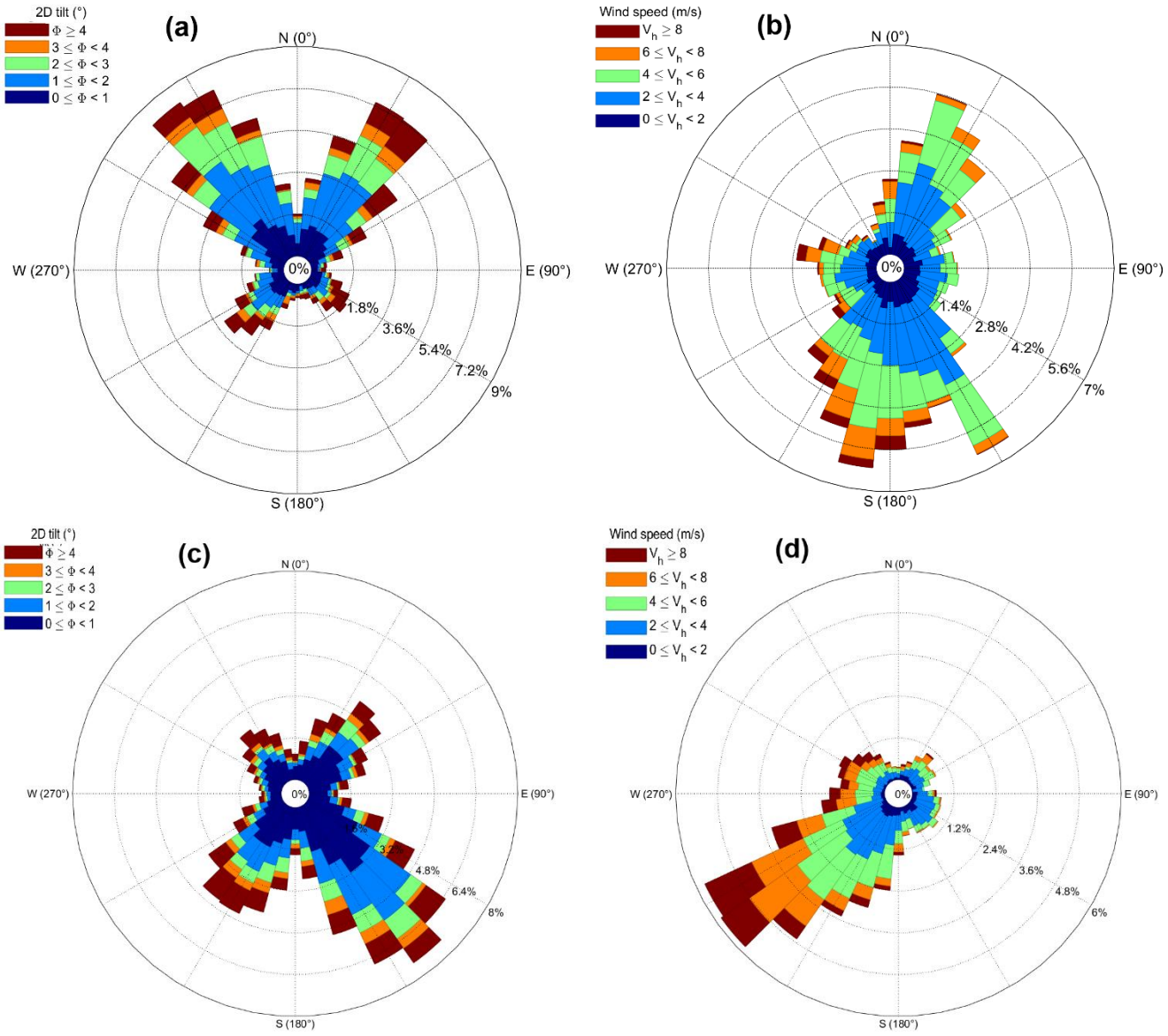

Figure S6. (left column) Rose of the two-dimensional inclination angle Φ for the medium search interval and (right column) wind rose at the first level of the reconstructed profile, for the site of (top line) Pari and (bottom line) Dunkerque.

S4. Additional case studies for the Paris inland site

Figure S7 presents the results of both wind reconstruction methods for an autumn day with a limited PBL development (up to ~0.5 km), but a deep aerosol layer in the free troposphere (from 0.5 to 2.2 km). These two aerosol layers were separated by a cleaner air layer in which the DBS method strived to retrieve the horizontal wind for the whole day (Figure S7.b,d), while the cross-RHI method yielded much better results, particularly in the afternoon (Figure S7a,c). Aberrant horizontal speed values around 13 m/s were sporadically retrieved in the first gate of the DBS (before 09:00 and after 22:00 UTC, Figure S7.b). Besides, the absence of blind zone in the cross-RHI method allowed to distinguish the thin nocturnal PBL of ~150 m depth (before 08:00 UTC),a layer that is barely visible on the DBS. The cross-RHI method provided less observations than the DBS technique in the upper part of the aerosol layer (from 1.5 to 2.2 km altitude), but with a higher level of confidence. One can also note that a cloud was present in the morning around 3.7 km altitude.

Figure S8(a) shows the horizontal component of the turbulent kinetic energy for the same day as Figure S7. The values are globally low, on this day with limited PBL development. On the first night, the nocturnal low-level jet (NLLJ) weakened after 02:00 UTC (Figure S8.a), but the shear in direction between the nocturnal boundary layer and the residual layer persisted even after (Figure S8.c) and produced turbulence at the interface between the two layers (Figure S8.a). On the second night, another NLLJ developed, accompanied by the same shear in direction, and the development of the nocturnal PBL, underneath the NLLJ is visible on Figure S8(a). Finally, Figure S8(b) displays the number of points included in each layer (average between the meridional and zonal RHI sweeps). In the lowest layers (below 200 m above the lidar) more than 160 points were available, while values dropped progressively below the threshold of 30 in the aerosol layer located in the free troposphere.

Figure S9(a–d) presents the results of both wind reconstruction methods for a late summer day with a strongly convective PBL that developed up to 1.4 km in the afternoon. NLLJs were also present on both nights, with wind directions from the East to East-North-East, while the wind in the air mass below the jet is rather Northerly. Figure S9(e) displays the horizontal TKE during the same day, where the nocturnal PBL (depth of ~250 m above the lidar) and the convective PBL are clearly visible.

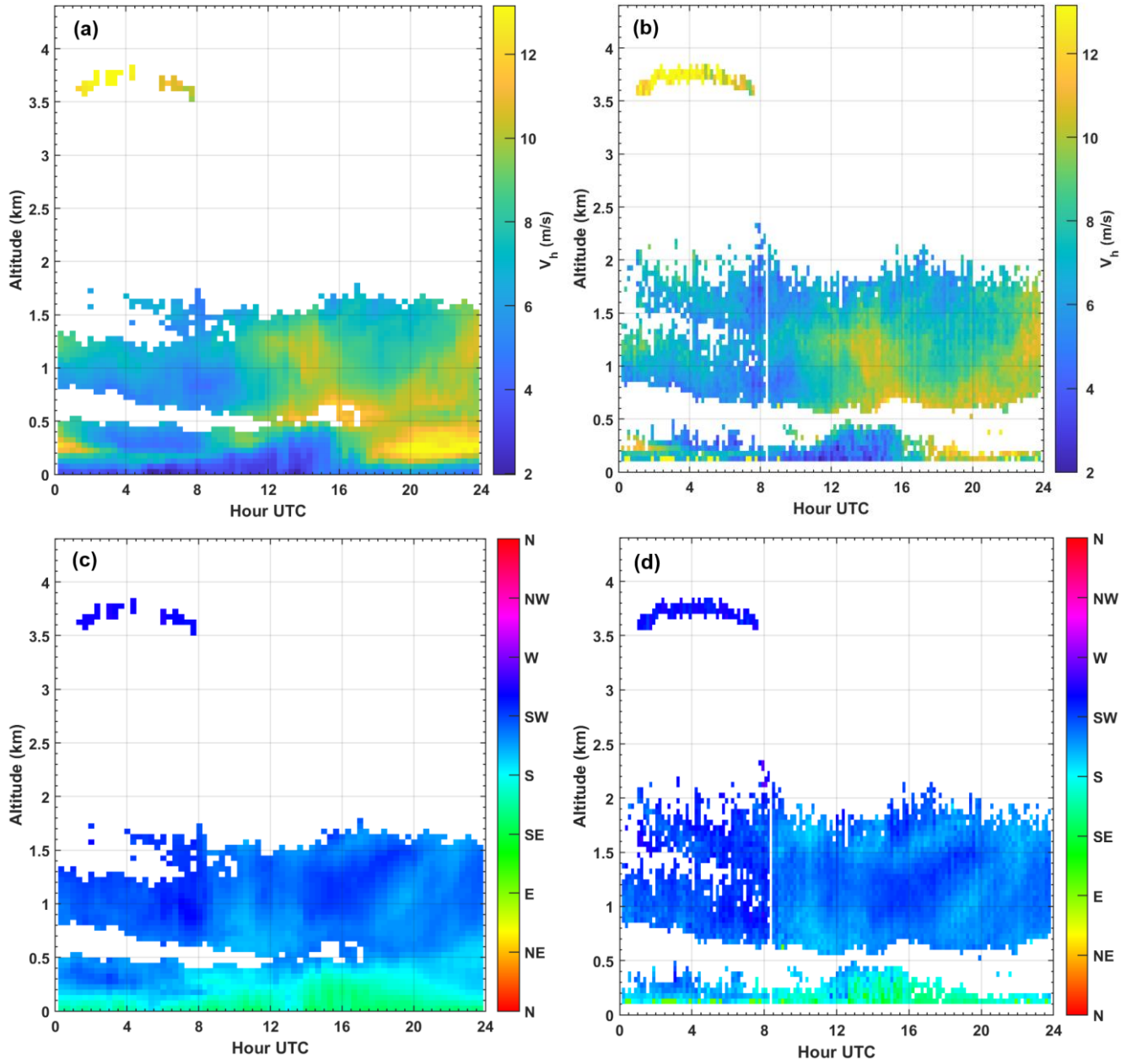

Figure S7. Time-altitude cross-section of the horizontal wind speed (a, b) and direction (c, d) retrieved over Paros on October 31st 2014 using the cross-RHI method (a, c) and the DBS technique (b, d). The colour scales are identical for the two wind speed and the two wind direction panels, respectively. The time resolution differs as DBS profiles were recorded twice during the measurement scenario (every 10 minutes), and cross-RHI pairs only once (every 20 minutes).

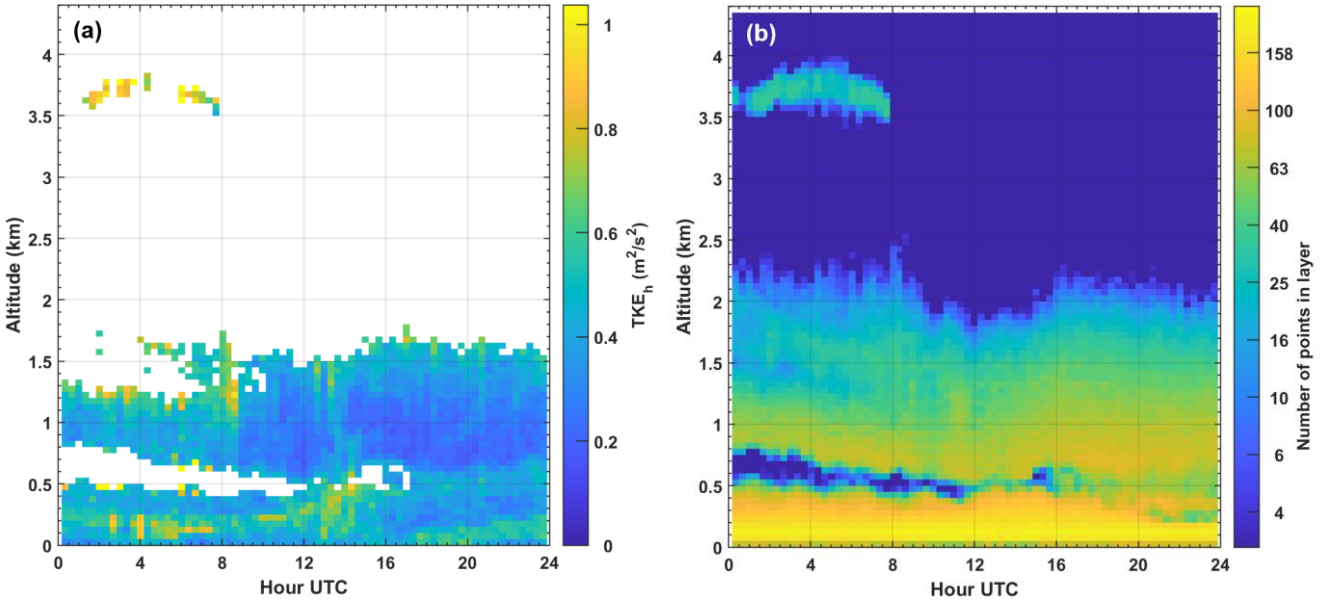

Figure S8. (a) Time-altitude cross-section of the horizontal component of the turbulent kinetic energy retrieved over Paris for October 31st 2014 using the cross-RHI method. (b) Number of points in each layer of the RHI reconstruction; the colour scale is logarithmic but the ticks' labels are the real numbers (the maximum value is 230).

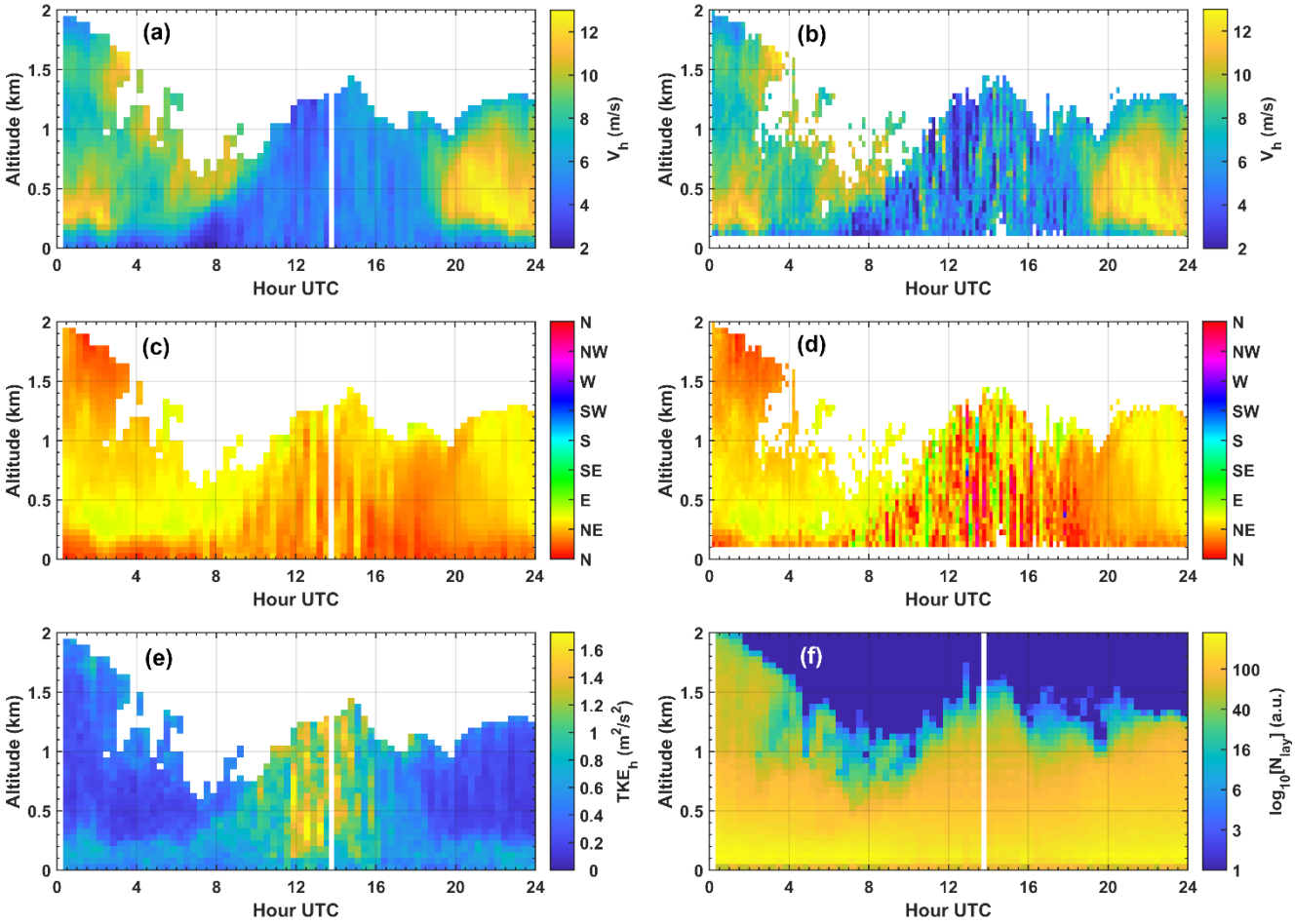

Figure S9. Same as Figure S7 and Figure S8, but on September 12th 2014: time-altitude cross-section of the horizontal wind speed (a, b) and direction (c, d) using the cross-RHI method (a, c) and the DBS technique (b, d) with identical colour scales for the two wind speed and the two wind direction panels, respectively. (e) time-altitude cross-section of the horizontal component of the turbulent kinetic energy retrieved using the cross-RHI method and (f) number of points in each layer of the RHI reconstruction.

S5. Cross-RHI to DBS statistical comparison in other altitude bands

S5.1. Comparison of the wind speed values

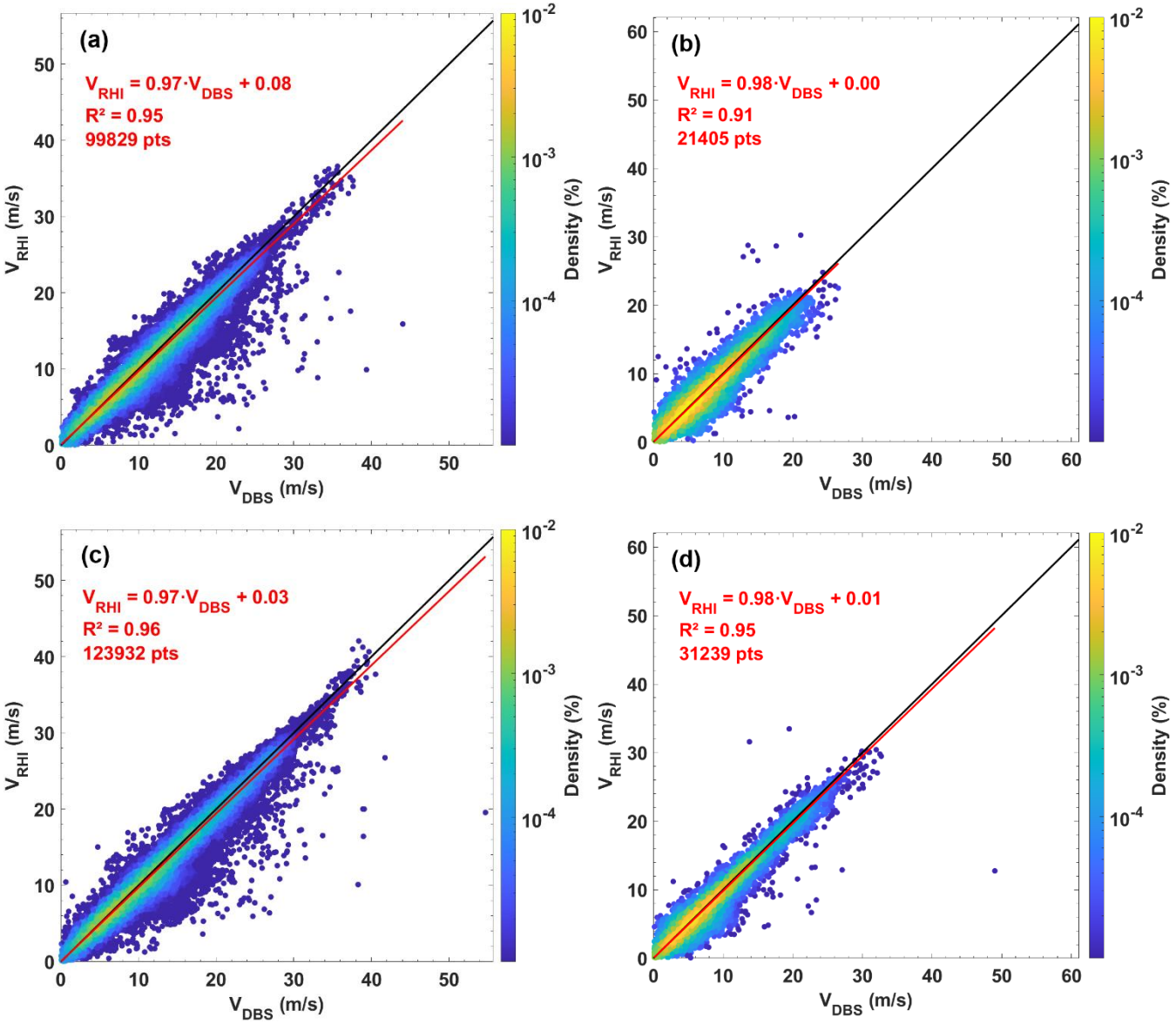

Figure S10. Scatter plot of the horizontal wind speed values retrieved by the DBS technique *vs* the cross-RHI method in Dunkerque (a,c) and Paris (b,d). For each site, the figures include data from the whole period indicated in Table 1, and for all altitudes between 0.2 and 0.5 km above the lidar (a,b) or between 0.5 and 1.0 km (b,d). The black and red lines represent the 1:1 line and the result from the orthogonal regression respectively. The colour scale represents the density of points, expressed as a fraction of their total number, in log scale.

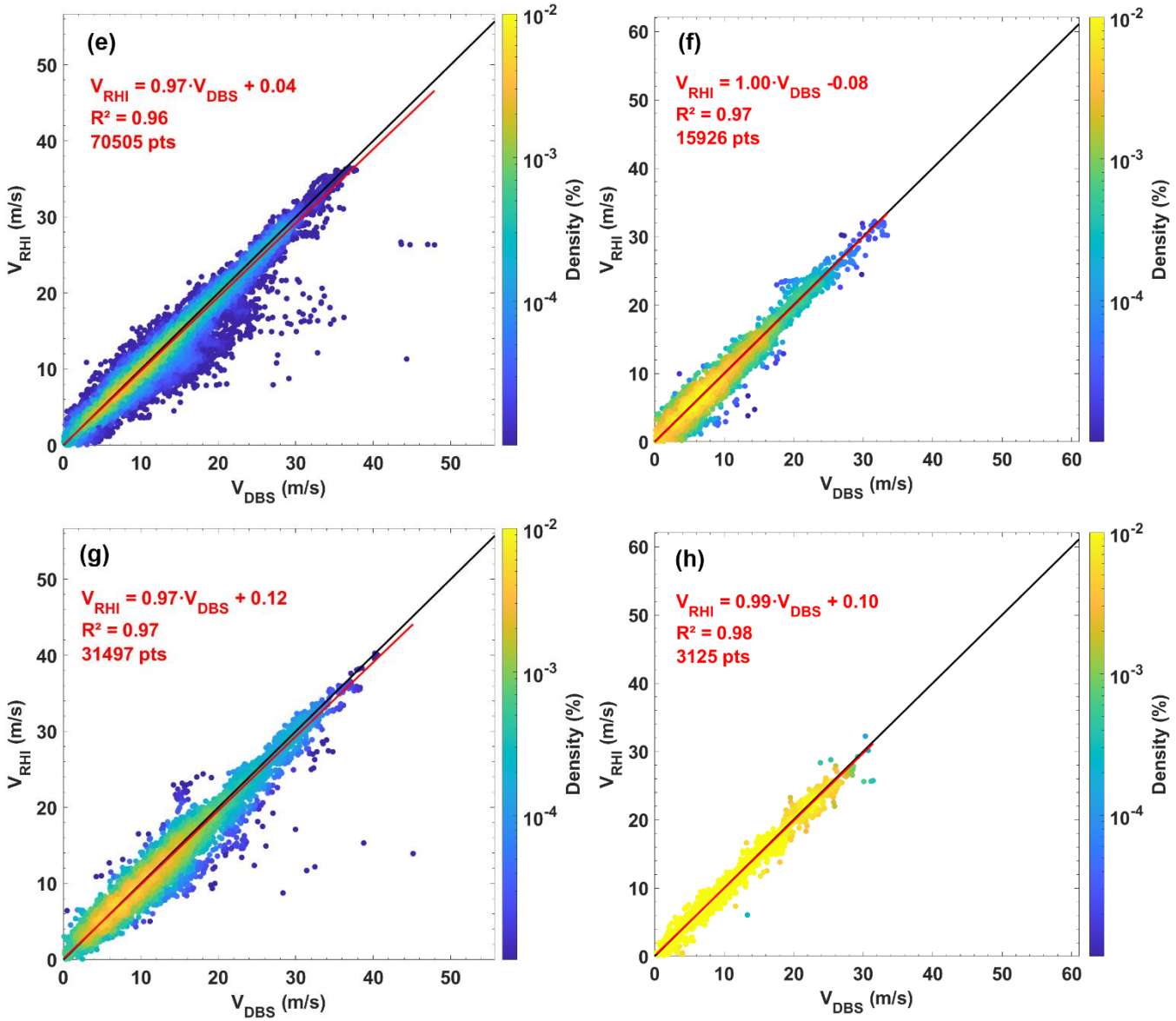

170 **Figure S10 (continued). Comparison of the horizontal wind speed from the cross-RHI and DBS methods in Dunkerque (e,g) and Paris (f,h), for the altitudes between 1.0 and 1.5 km above the lidar (e,f) and between 1.5 and 2.0 km (g,h).**

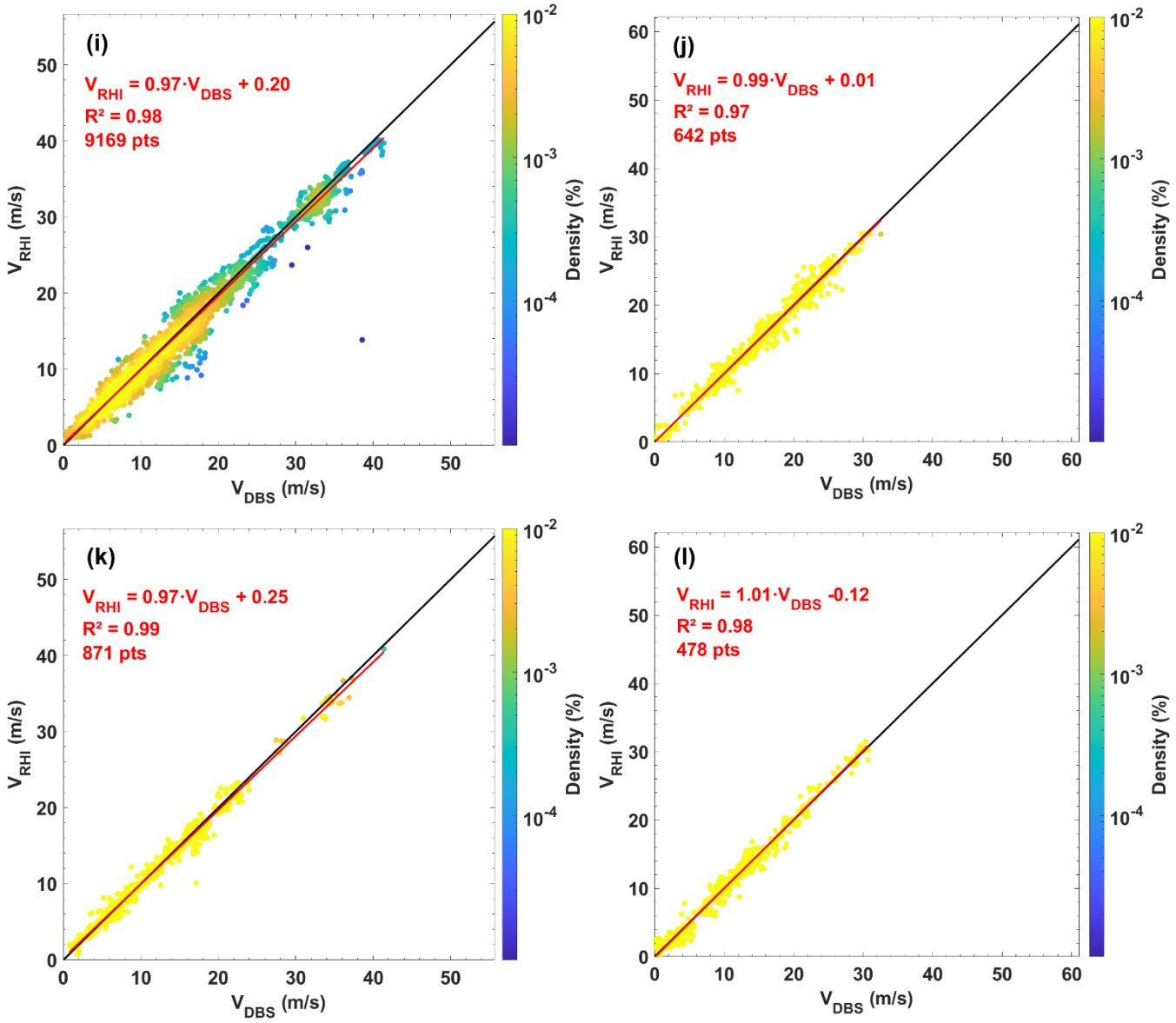

Figure S10 (continued). Comparison of the horizontal wind speed from the cross-RHI and DBS methods in Dunkerque (i,k) and Paris (j,l), for the altitudes between 2.0 and 2.5 km above the lidar (i,j) and between 2.5 and 3.0 km (k,l).

S5.2. Comparison of the wind direction values

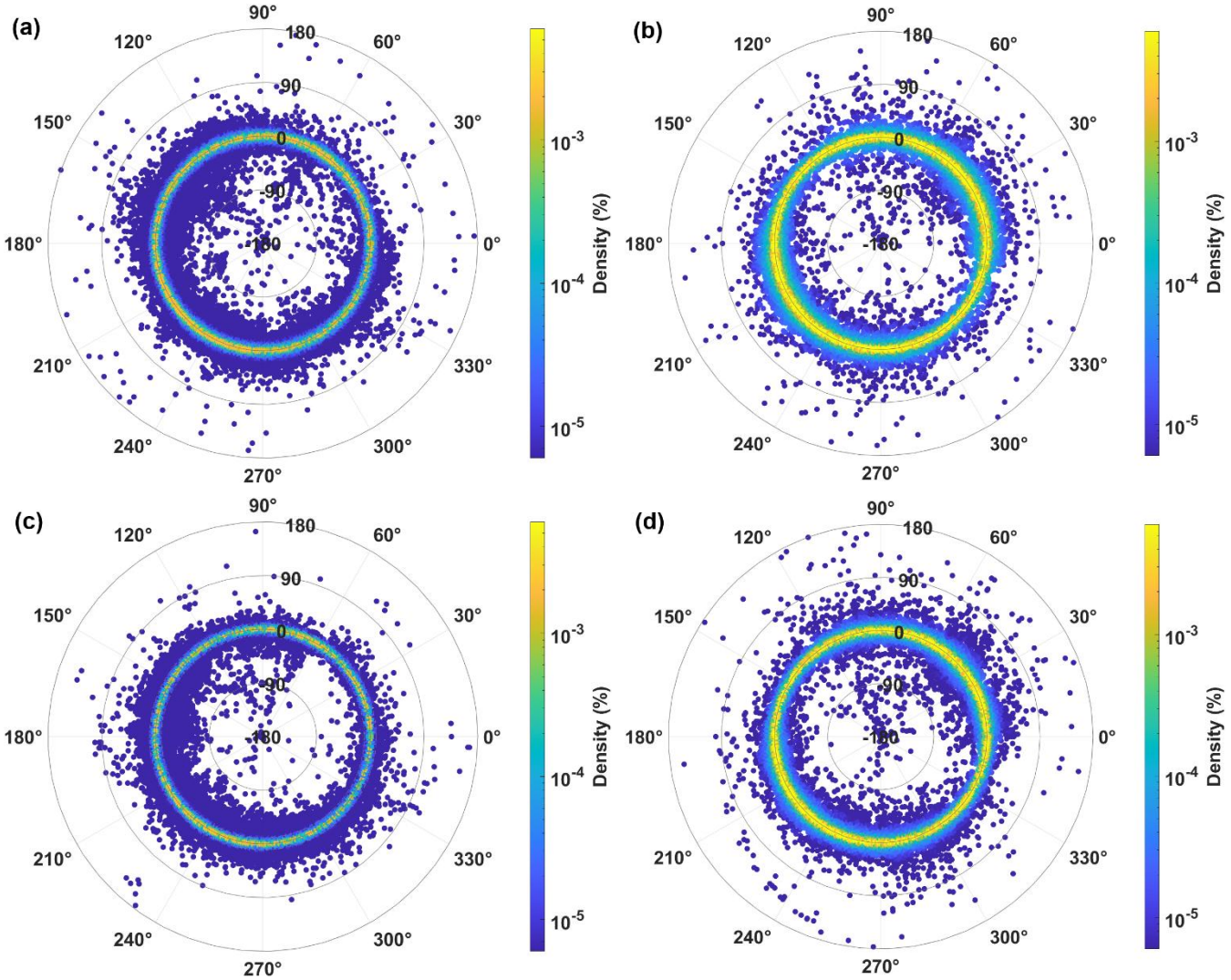

Figure S11. Horizontal wind direction difference (cross-RHI minus DBS) plotted as a function of the cross-RHI wind direction, in polar coordinates, for (a,c) Dunkerque and (b,d) Paris. For each site, the figure includes data from the whole period indicated in Table 1, and for all altitudes between 0.2 and 0.5 km above the lidar (a,b) or between 0.5 and 1.0 km (b,d). The colour scale represents the density of points, expressed as a fraction of their total number, in log scale.

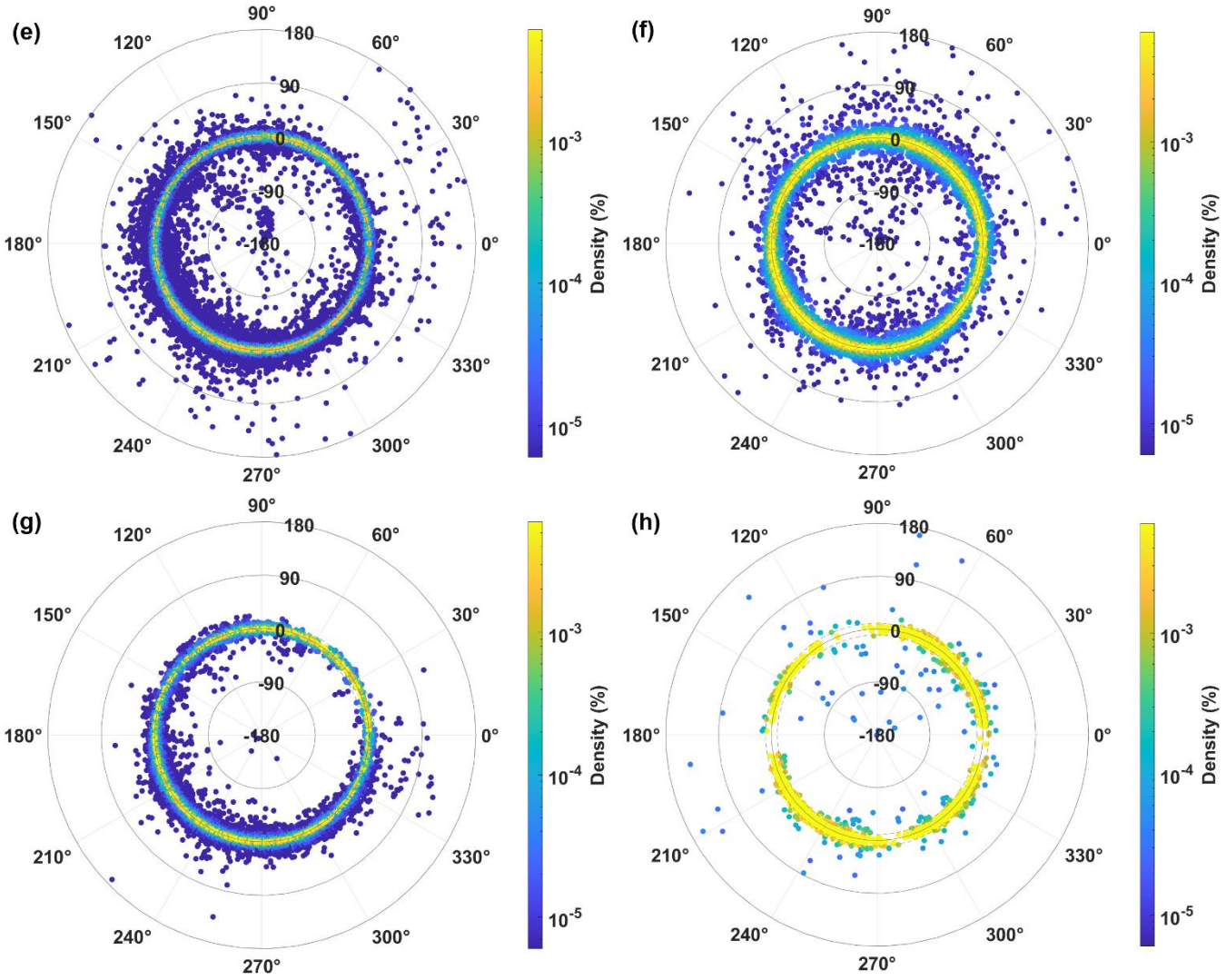

Figure S11 (continued). Comparison of the horizontal wind direction from the cross-RHI and DBS methods in Dunkerque (e,g) and Paris (f,h), for the altitudes between 1.0 and 1.5 km above the lidar (e,f) and between 1.5 and 2.0 km (g,h).

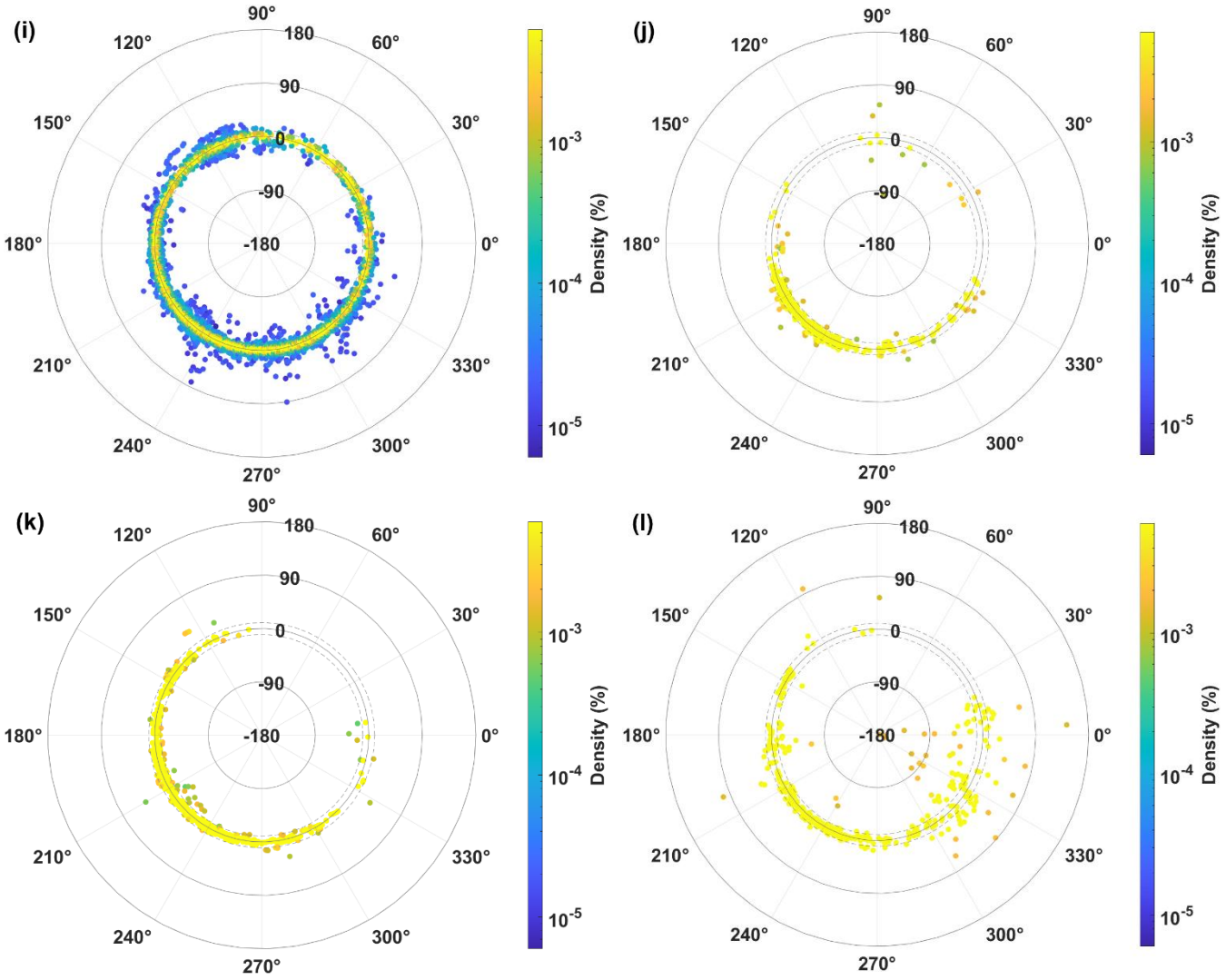

Figure S11 (continued). Comparison of the horizontal wind direction from the cross-RHI and DBS methods in Dunkerque (i,k) and Paris (j,l), for the altitudes between 2.0 and 2.5 km above the lidar (i,j) and between 2.5 and 3.0 km (k,l).

S6. Horizontal TKE comparison with and without layer inclination

Figure S12 displays the scatter plot of the TKE_h values computed with the layers' inclination optimization ($TKE_{RHItilt}$) *vs* the values computed without the optimization (TKE_{RHI}). TKE_h values are expected to decrease when taking into account the flow inclination. However, as the optimization concerned the average TKE_h in a wide altitude band, individual TKE_h values at a given altitude may actually increase when inclining the layers in the retrieval, yielding points also above the 1:1 line. Data is processed in log scale so that low and high TKE_h values, that cover several orders of magnitude, have an equal weight in the fitting process. The fit slope is fixed to unity, as in Bonin et al. (2017). If the y variable depends upon the x variable with a

unity slope, then the linear fit equation is $y = x + b$, with b the intercept. When computing the average, it comes $\bar{y} = \bar{x} + b$, so that $b = \bar{y} - \bar{x}$, i.e. the intercept is simply the difference between the averages. When comparing the horizontal TKE values with and without the layer's inclination optimization, $y = \log_{10}(\mathrm{TKE_{RHItilt}})$ and $x = \log_{10}(\mathrm{TKE_{RHI}})$, so that :

$$b = \langle \log_{10}(\mathrm{TKE_{RHItilt}}) \rangle - \langle \log_{10}(\mathrm{TKE_{RHI}}) \rangle = \langle \log_{10}\left(\frac{\mathrm{TKE_{RHItilt}}}{\mathrm{TKE_{RHI}}}\right) \rangle = \langle \eta \rangle \quad \text{(F1)}$$

Where the angle brackets denote the average over the ensemble of measurement points. The fit equations indicated on Figure S12 are in linear scale, so the slope corresponds to 10^b because $\mathrm{TKE_{RHItilt}} = 10^y = 10^{x+b} = 10^x \cdot 10^b = \mathrm{TKE_{RH}} \cdot 10^b$.

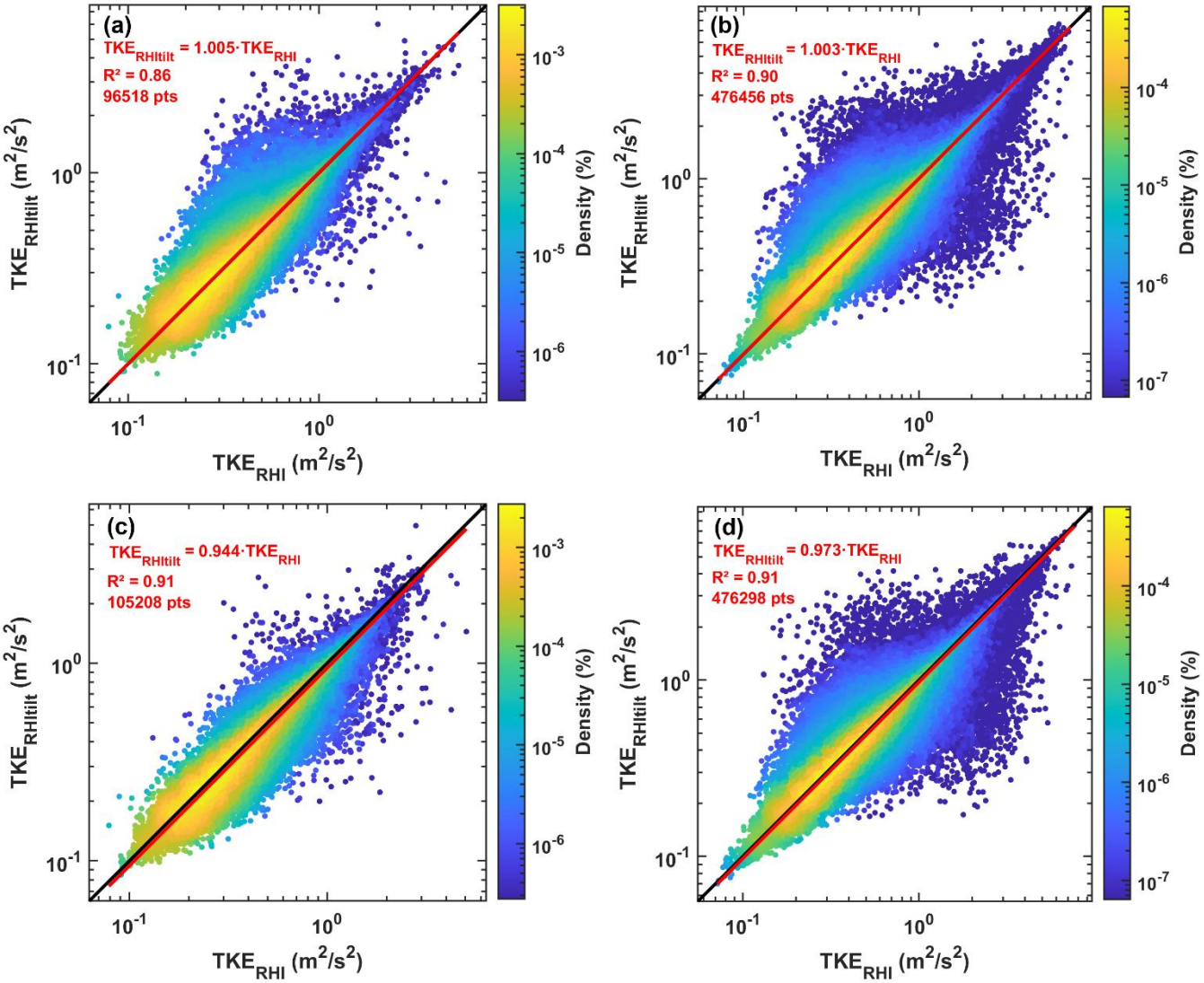

Figure S12. Scatter plot of the horizontal component of the TKE reconstructed using horizontal layers (x-axis) or using optimized inclined layers (y-axis), for the sites of (a, c) Paris and (b, d) Dunkerque. The optimization was performed over the lowest (a, b) 0.5 km and (c, d) 1.5 km of the profile. Profiles for which the optimization was not successful were excluded and points from all altitudes were gathered. The black and red lines represent respectively the 1:1 line and the result of the unity-slope fit in log scale.

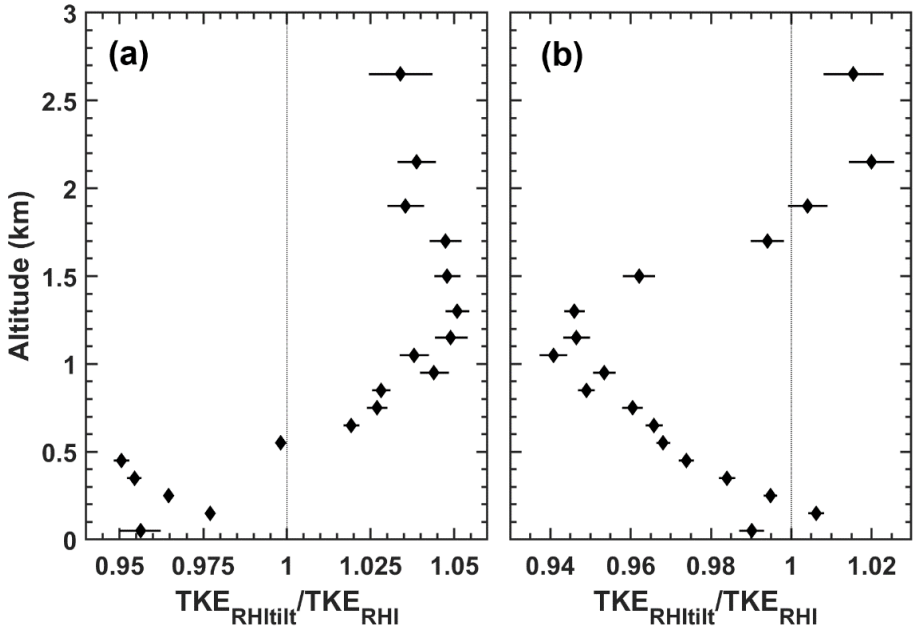

Figure S13. Variation of the bias (linear slope 10^b) with altitude, for the site of Dunkerque and for an optimization performed on the first (a) 0.5 km, and (b) 1.5 km of the horizontal TKE profile, i.e. N_{lay} equal to 20 or 60, respectively. The altitude band are 100 m wide up to 1.2 km, 200 m wide from 1.2 to 2.0 km, 300 m wide just above 2 km, and all data above 2.3 km are bind together (there was almost no observation above 2.6 km). The uncertainties (horizontal lines) correspond to the 95 % stationary-bootstrap confidence interval on the bias (diamonds).

References

Bonin, T. A., Choukulkar, A., Brewer, W. A., Sandberg, S. P., Weickmann, A. M., Pichugina, Y. L., Banta, R. M., Oncley, S. P., and Wolfe, D. E.: Evaluation of turbulence measurement techniques from a single Doppler lidar, Atmos. Meas. Tech., 10, 3021–3039, https://doi.org/10.5194/amt-10-3021-2017, 2017.

Cheliotis, I., Dieudonné, E., Delbarre, H., Sokolov, A., Dmitriev, E., Augustin, P., Fourmentin, M., Ravetta, F., and Pelon, J.: Properties of coherent structures over Paris: a study based on an automated classification method for Doppler lidar observations, J. Appl. Meteorol. Clim., 60, 1545–1559, https://doi.org/10.1175/JAMC-D-21-0014.1, 2021.

Newman, J. F., Klein, P. M., Wharton, S., Sathe, A., Bonin, T. A., Chilson, P. B., and Muschinski, A.: Evaluation of three lidar scanning strategies for turbulence measurements, Atmos. Meas. Tech., 9, 1993–2013, https://doi.org/10.5194/amt-9-1993-2016, 2016.